Quantum error detection in qubit-resonator star architecture

Florian Vigneau, ¹ Sourav Majumder, ¹ Aniket Rath, ¹ Pedro Parrado-Rodríguez, ² Francisco Revson Fernandes Pereira, ¹ Stefan Pogorzalek, ¹ Tyler Jones, ¹ Nicola Wurz, ¹ Michael Renger, ¹ Jeroen Verjauw, ¹ Ping Yang, ¹ Hsiang-Sheng Ku, ¹ William Kindel, ¹ Frank Deppe, ¹ and Johannes Heinsoo³

¹ IQM Quantum Computers, Georg-Brauchle-Ring 23-25, 80992 Munich, Germany ² IQM Quantum Computers, P. de la Castellana 200, Madrid 28046, Spain ³ IQM Quantum Computers, Keilaranta 19, 02150 Espoo, Finland (Dated: March 18, 2025)

Achieving industrial quantum advantage is unlikely without the use of quantum error correction (QEC). Other QEC codes beyond surface code are being experimentally studied, such as color codes and quantum Low-Density Parity Check (qLDPC) codes, that could benefit from new quantum processing unit (QPU) architectures. Star-topology offers effective all-to-all connectivity in comparison to the square-grid topology and thus enables more hardware efficient implementation of some QEC codes. We encode two logical qubits in a star-topology superconducting QPU using the $[\![4,2,2]\!]$ code and characterize the logical states with the classical shadow framework. Logical life-time and logical error rate are measured over repeated quantum error detection cycles for various logical states including a logical Bell state. We measure logical state fidelities above 96 % for every cardinal logical state, find logical life-times above the best physical element, and logical error-per-cycle values ranging from 0.25(2) % to 0.91(3) %. The presented QPU configuration can be used to enable qubit-count efficient QEC codes via the high connectivity in future devices.

I. INTRODUCTION

There are industrially relevant computational tasks which can be solved faster, cheaper, or more accurately using quantum computers, but achieving industrial quantum advantage likely require error rates only accessible by means of quantum error correction (QEC) [1, 2]. In stabilizer based QEC [3, 4], two-qubit gates are used to map data-qubit parity to ancilla qubit states [5]. Repeated measurements of the ancilla qubit states provide error syndrome data, which can be decoded to identify likely errors and extend the lifetime of the logical qubit. Logical error rates depend on the physical quantum gate fidelity, the physical qubit lifetime, the topological properties of the used code, and also on the match between code structure and architecture of the QPU. While the planar square grid of superconducting qubits fits well the stabilizers of surface code [5–8], there are other stabilizer circuits and codes such as planar color codes [9] and qLDPC codes [10, 11], which could outperform surface code on other QPU architectures in terms of logical error rate for a given number of physical qubits [12].

Compared to surface codes, large-distance color codes have additional requirements [13, 14]. First, they require the measurement of at least weight-six stabilizers. Secondly, X and Z basis stabilizers are supported by the same data qubits. Thus, color codes do not map to a locally connected 2D array of qubits in a trivial way. This difficulty has been overcome in quantum computers based on trapped ions [15, 16], where two-qubit gates are possible between qubits that share a vibrational mode of the trap, and on neutral atoms [17, 18], where atoms can be shuttled around modifying the effective connectivity during operation. With superconducting qubits, individual stabilizers of color code have been demonstrated on a five qubit device [19–21] and a mapping of color code has

been proposed for the heavy-hex architecture [22] where extra two-qubit gates and qubits were employed for routing and measuring syndrome-circuit error flags. Recently, a distance-three color code has been demonstrated on a square grid architecture [23] using a superdense coding circuit [12].

The smallest possible color code is the [4,2,2] code [24-27], which encodes two logical gubits in four data gubits. The code allows correction of erasure errors and detection of up to one error on the data gubits. This code has been employed in the early error detection experiments with modest size QPUs [19, 28–32]. It has been used to demonstrate variational quantum eigensolver algorithms with increased accuracy [33, 34] and magic state injection [35]. The code allows logical single- and two-qubit gates within the same patch with simple physical level operations [36]. Recently, using the same code, a 24-logical-qubit cat state was prepared using 12 pairs of logical qubits encoded in the state of 256 neutral atoms [37].

To enable scalable qubit- and gate-count-efficient encoding of superconducting qubits with color and qLDPC codes, increased connectivity is needed. We report quantum error detection with a star topology QPU featuring a resonator, as a central computational element, connected to six transmon qubits via tunable couplers [38]. This topology increases the connectivity between qubits in a sense that there is an element which is coupled to more than four neighbors. We demonstrate logical error detection by encoding two logical qubits with the [4, 2, 2]code. We describe the circuit, characterize the stabilizer and use the classical shadow technique [39, 40] to measure the quality of the logical state encoding. We then repeat the error detection cycle to measure the logical state decay. Finally, we encode a logical Bell state in the two logical qubits.

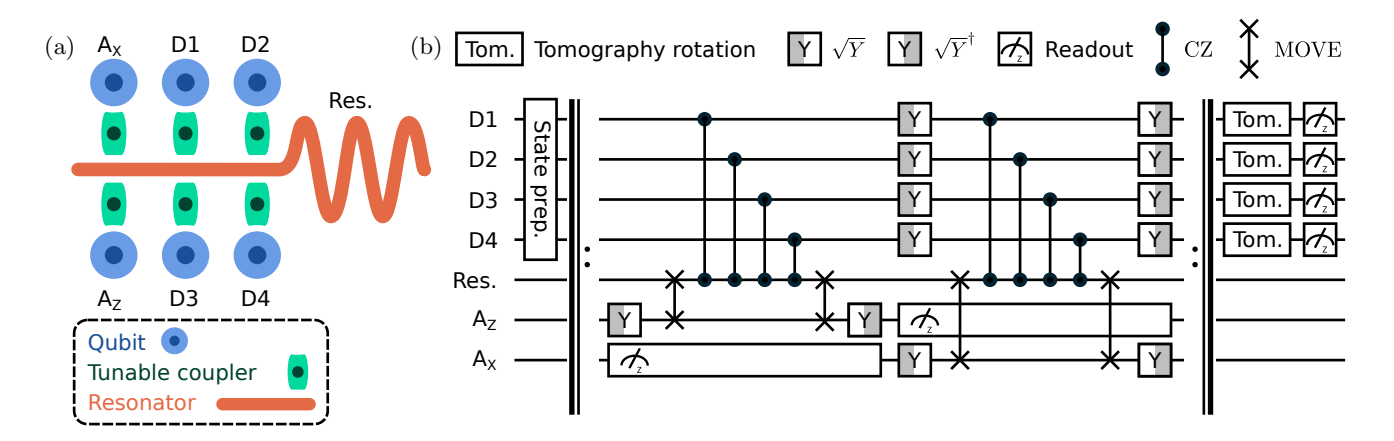


FIG. 1. a) Schematic of the QPU featuring four data qubits (D1–D4) and two ancilla qubits (A_X and A_Z) connected via tunable couplers (green) to a central resonator (Res., orange). b) Gate sequence of the distance-2 error detection cycle consisting of state preparation sub-circuit; stabilizer measurement cycles implemented with single qubit \sqrt{Y} gates, its inverse \sqrt{Y}^{\dagger} , resonator-qubit CZ and MOVE gates and ancilla qubit measurements; single qubit gates for state tomography and final data qubit readout operations, see App. B.

II. DESCRIPTION OF THE ERROR DETECTION SCHEME

Our QPU, illustrated in Fig. 1a, features six transmon qubits, each connected by a tunable coupler to the central resonator. We use four data qubits D1-D4 to encode two logical states and the two remaining qubits $A_{\rm X}$ and $A_{\rm Z}$ as ancillas for error syndrome detection.

The code is defined by the stabilizers

$$S_{X} = X_{D1}X_{D2}X_{D3}X_{D4},$$

$$S_{Z} = Z_{D1}Z_{D2}Z_{D3}Z_{D4},$$
(1)

where X_i and Z_i are Pauli operators for qubit i, and by the logical operators of the two logical qubits

$$X_{L1} = X_{D3}X_{D4} , Z_{L1} = Z_{D1}Z_{D3}, X_{L2} = X_{D2}X_{D4} , Z_{L2} = Z_{D1}Z_{D2},$$
 (2)

which in turn define the logical codewords that relate the physical states to the logical states, see App. A.

The physical gate circuits studied in this paper consist of state preparation, stabilizer measurement cycle and data qubits readout, see Fig. 1b. State preparation circuit varies for experiments described in this paper. For encoding separable logical states, we prepare the data qubits in an initial state $\psi_{\rm in}$ that overlaps with a single codeword $\psi_{\rm target}$ using natural qubit decay and single-qubit gates before the first cycle. Then, in the absence of errors, the first measurement of the stabilizers projects the data qubits to the corresponding codeword state with 1/2 probability (probabilistic encoding strategy). State preparation for the logical Bell state is described in Sec. VI.

Our stabilizer measurement circuit consists of 12 single-qubit \sqrt{Y} gates, ten qubit-resonator gates, and two ancilla qubit readout operations, see Fig. 1b. First, \sqrt{Y}

gates are used to change between Z and X basis. Then a MOVE operation is used to transfer the state from an ancilla qubit to the central resonator, where MOVE is similar to an iSWAP gate, but limited to the state-space spanned by $|0q\rangle$, $|1q\rangle$, $|0e\rangle$ states of the resonator-qubit subsystem [38]. Next, CZ gates are successively applied between data qubits and the central resonator. Finally, the state is moved back to the ancilla gubit with a second MOVE. The ancilla qubit is then measured to obtain the value of the stabilizer. A similar gate sequence is realized with the second ancilla to measure the other stabilizer. This second sequence can be executed while the first ancilla qubit is being measured, following an interleaved measurement scheme inspired by Ref. [41]. At the end of N error detection cycles, data qubits are measured. In the tomography experiments, combinations of single qubit gates from the set $\{I, \sqrt{X}, \sqrt{Y}\}\$ are applied before data qubit readout.

This circuit for stabilizer measurement is not fault tolerant in a sense that a single bitflip error in the computational resonator or ancilla qubit in the middle of the syndrome extraction circuit can lead to an undetectable logical error. Adding an additional qubit as a flag would allow detecting these errors [42]. However, for higher distance color codes, there are syndrome extraction circuits without error flags which outperform a circuit with imperfect-flags as well as surface code for the same resources and error model [12]. Thus, it is still an open question which circuit and architecture is optimal for future QEC codes.

III. STABILIZER CHARACTERIZATION

We characterize the performance of the stabilizers measurement circuits by measuring the expectation values of the individual stabilizers in a single stabilizer tomogra-

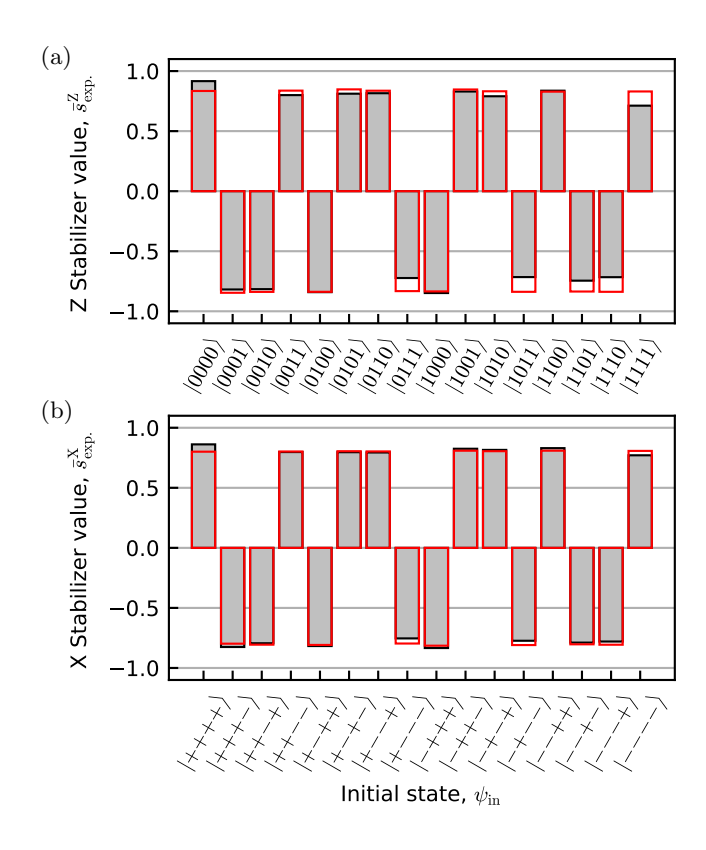


FIG. 2. Single stabilizer measurement expectation values $\bar{s}_{\text{exp.}}^{Z}$ (a) and $\bar{s}_{\text{exp.}}^{X}$ (b) for initial state ψ_{in} , averaged over 10^{5} repetitions from experiment (gray) and error-model simulation (red). $|\pm\rangle = (|0\rangle \pm |1\rangle)/\sqrt{2}$.

phy experiment [43]. We study a single stabilizer at a time by executing only first or second half of the circuit of the cycle given in Fig. 1b. We repeat the experiment with 16 separable states $\psi_{\rm in}$ which form an eigenbasis of the studied stabilizer such that we expect to measure $s_{i,{\rm ideal}} = \langle \psi_{i,{\rm in}} | S | \psi_{i,{\rm in}} \rangle = \pm 1$. The observed stabilizer values averaged over experiment repetitions $\bar{s}_{\rm exp.}$, see Fig. 2, are well reproduced by the individually characterized errors, detailed in App. H. We observe a stabilizer fidelity [43] $1 - \langle |\bar{s}_{i,{\rm exp.}} - s_{i,{\rm ideal}}| \rangle/2 = 90.1\%$ averaged over the input states $\psi_{i,{\rm in}}$ for $S_{\rm X}$ and 89.8% for $S_{\rm Z}$.

IV. QUANTUM STATE TOMOGRAPHY

We perform tomography experiments to understand the performance of the logical and physical state preparation. To derive unbiased estimations of quantities of interest in this work, we employ the framework of classical shadows, also known as shadow tomography, based on local Pauli measurements [39, 40], see App. C for further information.

In this experiment, we prepare $\psi_{\rm in}$ from the set of 16 separable states, for which either $\langle \psi_{\rm in} | S_{\rm X} | \psi_{\rm in} \rangle = 1$ or $\langle \psi_{\rm in} | S_{\rm Z} | \psi_{\rm in} \rangle = 1$. Then, we measure both stabilizers once using the full circuit given in Fig. 1b. Thereafter,

$\psi_{ m in}$	ψ_{target}	$F_{ m L}$	$p_{2,\mathrm{L}}$	$p_{2,\mathrm{phy}}$	$P_{ m L}$	$P_{ m S}$
$ 0000\rangle$	$ 00\rangle_{ m L}$	0.989	0.876	0.322	0.723	0.848
$ 1111\rangle$	$ 00\rangle_{ m L}$	0.992	0.880	0.299	0.714	0.832
$ 0011\rangle$	$ 01\rangle_{ m L}$	0.978	0.855	0.294	0.714	0.874
$ 1100\rangle$	$\ket{01}_{ m L}$	0.993	0.879	0.295	0.713	0.852
$ 0101\rangle$	$ 10\rangle_{ m L}$	0.979	0.853	0.293	0.730	0.526
$ 1010\rangle$	$ 10\rangle_{ m L}$	0.975	0.848	0.289	0.721	0.862
$ 0110\rangle$	$ 11 angle_{ m L}$	0.999	0.918	0.285	0.606	0.852
$ 1001\rangle$	$\ket{11}_{ m L}$	0.982	0.872	0.289	0.667	0.878
	$\ket{++}_{ m L}$	0.978	0.854	0.268	0.677	0.848
$ ++++\rangle$	$\ket{++}_{ m L}$	0.968	0.837	0.274	0.694	0.902
$\ket{+-+-}$	$\ket{+-}_{ m L}$	0.966	0.831	0.274	0.709	0.648
$ -+-+\rangle$	$\ket{+-}_{ m L}$	0.981	0.857	0.278	0.698	0.870
$ ++\rangle$	$\ket{-+}_{ m L}$	0.993	0.882	0.276	0.681	0.676
$\ket{++}$	$\ket{-+}_{ m L}$	0.981	0.861	0.274	0.682	0.870
$\ket{++}$	$_{ m L}$	0.966	0.834	0.274	0.693	0.846
$ -++-\rangle$	$ angle_{ m L}$	0.968	0.836	0.277	0.702	0.904

TABLE I. Summary of results extracted from shadow tomography for different initial physical states $\psi_{\rm in}$ that encode logical states $\psi_{\rm target}$ in X and Z basis respectively.

for each initial state, we apply to the data qubits all of the $3^4=81$ combinations of single-qubit Pauli tomography gates. For each instance of these rotations, we repeat the experiment 2×10^3 times.

The measurement data is post-selected conditioned on the result of both stabilizer measurements $s^{\rm Z}$ and $s^{\rm X}$ yielding a value of +1. Due to our choice of input and target states, we would reject 50% of states even in the ideal case. In addition, there are errors in data qubits and stabilizer circuit resulting in stabilizer acceptance probability $P_{\rm S} \in [0.65, 0.90]$, see Table I, and total post selection yield is $P_{\rm S}/2$.

We construct the density matrix of the logical state $\rho_{\rm L} = \sum_{i,j} \left\langle i \middle| \rho_{\rm phy} \middle| j \right\rangle / P_{\rm L}$ by projecting the physical state $\rho_{\rm phy}$ onto the logical subspace $|i\rangle$, $|j\rangle \in \{ |00\rangle_{\rm L} \,, |01\rangle_{\rm L} \,, |10\rangle_{\rm L} \,, |11\rangle_{\rm L} \, \}$ with logical acceptance probability $P_{\rm L} = \left\langle i \middle| \rho_{\rm phy} \middle| i \right\rangle$ [7]. Finite probability $P_{\rm L} \in [0.606, 0.730]$ indicates that there are errors not captured by syndrome measurements. The probability $P_{\rm L}$ also relates logical and physical state fidelity $F_{\rm L} = \left\langle \psi_{\rm target} \middle| \rho_{\rm L} \middle| \psi_{\rm target} \right\rangle = F_{\rm phy} / P_{\rm L} \, [7, \, 44]$. We observe logical fidelity $F_{\rm L} > 0.965$ for all the prepared two-qubit logical states. Slightly lower fidelities for X basis states arise from the additional single qubit gates required to prepare $\psi_{\rm in}$. The total success probability of producing and measuring a state in the logical subspace is $\eta = (1/2)P_{\rm S}P_{\rm L}$.

Purity of the logical state $p_{2,L} = \text{Tr}(\rho_L^2) \in [0.83, 0.92]$ indicates finite probability of always preparing the same logical state. As physical state purity $p_{2,\text{phy}} \in [0.27, 0.32]$, is considerably lower than $p_{2,L}$ for all input states, we have confirmed that projection to the logical subspace rejects states prepared out of logical subspace.

The reconstructed physical and logical density matrices obtained by quantum state tomography are shown in

V. REPEATED ERROR DETECTION

Next, to obtain the logical lifetime and error rate, we conduct lifetime experiments with four target X and Z basis states, by preparing $|0000\rangle$, $|0011\rangle$, $|0101\rangle$, $|1001\rangle$, $|++++\rangle$, $|+-+-\rangle$, $|++--\rangle$ and $|-++-\rangle$ with $|\pm\rangle=(|0\rangle\pm|1\rangle)/\sqrt{2}$. We repeat the error detection cycle $N=\{1,\ldots,20\}$ times. For each error detection cycle $n\leq N$, we measure both stabilizers s_n^Z and s_n^X . After N cycles, we measure the data qubit states in the same basis as the preparation. We post-select the measurement results based on the stabilizers and data qubits being assigned to the logical subspace before evaluating $\langle X_{\text{L}i}\rangle_N$ and $\langle Z_{\text{L}i}\rangle_N$ of logical qubit i from 10^5 experiment repetitions. For comparison, we simulate 10^6 repetitions of the experiment with Stim [45], see App. H for details.

We find that the number of accepted runs follows an expected relation $\eta_N = P_{\rm S}^N P_{\rm L} / 2$ and agrees with the simulation, see Fig. 3a and Fig. 3b. We estimate $P_{\rm S} = \eta_N/\eta_{N-1} \approx 0.67$ and $P_{\rm L} = 2\eta_1/P_{\rm S} \approx 0.87$. These values are consistent with those derived from the tomography experiments in the previous section.

Also, the decay dynamics of the expectation values of $Z_{\rm L1}, Z_{\rm L2}, X_{\rm L1}$ and $X_{\rm L2}$ agrees with the simulation. We fit a function $ae^{-N\cdot b}$, where a and b are free parameters and use the successful run fraction η_N to weight the data points, see Figs. 3c-f. We calculate logical lifetime $\tau_{\rm Z}=t_{\rm cycle}/b\in[138,407]$ µs from the experiment in Z basis and logical coherence time $\tau_{\rm X}\in[111,249]$ µs for X basis, see Table II. The observed logical life- and coherence times are all improved compared to the best physical component, see App. G.

From the fitted parameters, we also obtain the error rate, logical error per cycle $\varepsilon = (1-e^{-b})/2$, which corresponds to a decay of the expectation value $\langle X_{\text{L}i} \rangle_{N+1} = (1-2\varepsilon_{Xi}) \langle X_{\text{L}i} \rangle_{N}$ and similar for Z_{L} [46]. The error rate ranges from $\varepsilon_{\text{Z}1} = 0.25\,\%$ for $|10\rangle_{\text{L}}$ to $\varepsilon_{\text{Z}1} = 0.91\,\%$ for $|-+\rangle_{\text{L}}$, see Table II. All logical error rates are lower than error rate $1-F_{\text{cz}} \approx 1.03\,\%$ of the best CZ gate used in the experiment.

VI. LOGICAL BELL STATES

Here, we demonstrate preparation and preservation of entanglement for two logical qubits. Between the previous experiment and the following one, the device was thermally cycled and we exchanged the role of some of the physical qubits, see App. G.

We create a logical Bell state

$$|\Phi\rangle_{\rm L} = \frac{|00\rangle_{\rm D1\,D4} + |11\rangle_{\rm D1\,D4}}{\sqrt{2}} \otimes \frac{|00\rangle_{\rm D2\,D3} + |11\rangle_{\rm D2\,D3}}{\sqrt{2}}$$
(3)

State	$\tau_{\rm Z1}~(\mu \rm s)$	$\tau_{\rm Z2}~(\mu \rm s)$	$\varepsilon_{\mathrm{Z}1}$ (%)	$\varepsilon_{\mathrm{Z}2}~(\%)$
$ 00\rangle_{\rm L}$	175(9)	157(1)	0.58(3)	0.64(5)
$ 01\rangle_{ m L}$	303(15)	204(38)	0.34(2)	0.50(8)
$ 10\rangle_{ m L}$	407(34)	155(8)	0.25(2)	0.65(3)
$\ket{11}_{ m L}$	242(15)	138(12)	0.42(2)	0.73(6)
	$\tau_{\rm X1}~(\mu \rm s)$	$\tau_{\rm X2}~(\mu \rm s)$	$\varepsilon_{\mathrm{X1}}$ (%)	$\varepsilon_{\mathrm{X2}}$ (%)
$ ++\rangle_{\rm L}$	129(5)	190(7)	0.79(3)	0.53(2)
$\ket{+-}_{ m L}$	134(9)	192(24)	0.76(4)	0.53(6)
$\ket{-+}_{ m L}$	111(4)	178(14)	0.91(3)	0.57(4)
$ \rangle_{\rm L}$	153(8)	249(25)	0.66(3)	0.41(4)

TABLE II. Logical lifetime τ_{Zi} , coherence time τ_{Xi} , logical X_L and Z_L error probability ε_{Xi} and ε_{Zi} for logical qubit i for various logical states together with the uncertainty obtained from fit residuals.

by creating physical Bell states between the data qubits pairs D1–D4 and D2–D3 [27]. We prepare the physical Bell pairs with effective CZ gate between the qubit pair and \sqrt{Y} gates. Unlike previously, the $|\Phi\rangle_{\rm L}$ state is encoded by the state preparation circuit already before the first cycle of error detection. Therefore, the experiment does not suffer from rejection of half of the runs by the first stabilizer measurement. Together with the first stabilizer measurement, this state preparation scheme is as fault tolerant as the stabilizer circuit [27].

We repeat error detection cycles with postselection according to the stabilizer measurements and the final physical state being in the logical subspace. To address the decay of the number of post-selected results while also saving time on the experiment with small number of cycles N, we scale the number of experiment repetition according to $5 \times 10^3 N$ and $5 \times 10^4 N$ for simulation.

We see in experiments and simulations qualitatively the same trends of success probability η_N , see Fig. 4a. Apparently the success rate in the experiment outperforms our simulations quantitatively, which is likely due to changes in the performance between independent characterization and experiment. By fitting η_N to the experiment data, we find that on average $P_{\rm S}=71\,\%$ of the runs are kept after each cycle, which is slightly better than for separable logical states, with an acceptance probability $P_{\rm L}\approx 0.88$ close to the observation for other states (see Section V).

When measuring the Bell state in Z basis, we observe $|00\rangle_{\rm L}$ and $|11\rangle_{\rm L}$ states with a probability close to 0.5 each as expected, see Fig. 4b. We also plot the sum the observation probability of these two states, which an upper bound for probability of logical state $|\Phi\rangle_{\rm L}$. We observe general quantitative agreement between simulation and experiments. From an exponential fit to the experimentally obtain Bell state observation probability we obtain the logical life time $\tau_{\Phi}=400(30)$ µs and logical error per cycle $\varepsilon_{\Phi}=0.25(2)$ % which are comparable to the best preserved separable logical state.

However, Z basis measurement alone is not enough to

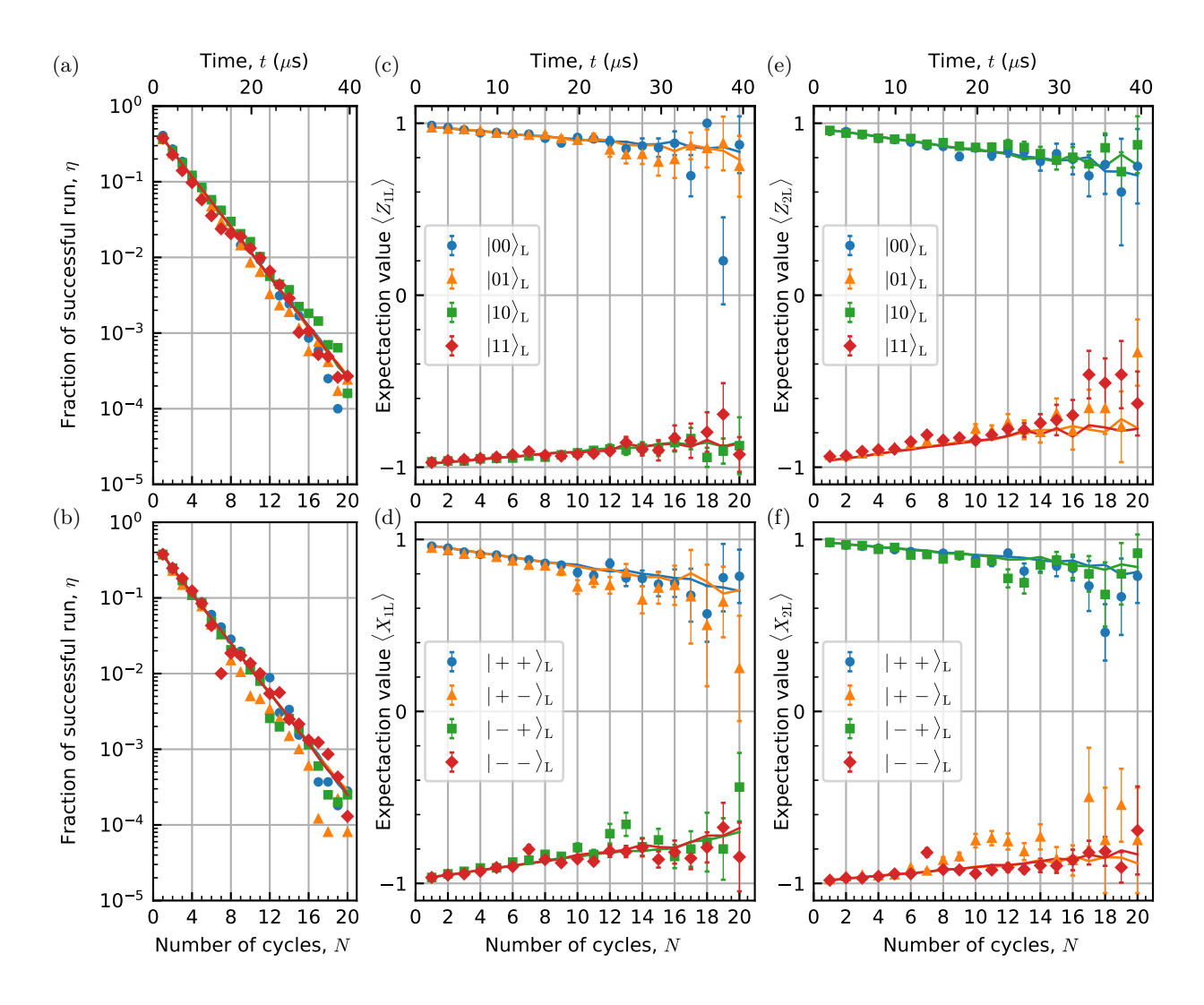


FIG. 3. a,b) Fraction of successful run η where no error have been detected versus number of cycle N and time t, for the logical states in caption. c-f) Expectation values of the logical operators Z_{L1} , Z_{L2} , X_{L1} and Z_{L2} versus number of cycle. The error bars are one standard deviation calculated considering a binomial distribution with η_N . Solid lines are simulations.

demonstrate entanglement between the two logical qubits as it cannot distinguish a Bell state from mixed states with classical correlations. To reveal the entanglement between the two logical qubits, we again conduct logical state tomography.

We first characterize the encoding circuit by conducting the tomography right after the initialisation of $|\Phi\rangle_{\rm L}$ state and before doing any error detection cycles, see App. D for the extracted density matrices. The logical fidelity $F_{\rm L}=0.995$, logical purity $p_{2,\rm L}=0.98$ and physical purity $p_{2,\rm phy}=0.676$ are higher than in the previous experiments due to lower number of used physical gates.

We also conduct tomography of the $|\Phi\rangle_{\rm L}$ state after up to N=15 cycles of error detection and post selection. We scale the number of repetition to 10^3N . We obtain the expected exponential decay of $F_{\rm L}$ with logical life time 100(5) µs and logical error rate $\varepsilon_{\Phi}=1.01(4)$ %, see Fig. 4c. Even after N=15 cycles fidelity $F_{\rm L}>0.5$

which indicates that the two logical qubits preserve entanglement. We also observe an exponential decay for the logical and physical purity as the state gets more and more mixed, with the exception of N=0 discussed before.

VII. CONCLUSION

We have encoded two logical qubits in using the $[\![4,2,2]\!]$ code in a state of six superconducting qubits arranged in a star topology with a central computational resonator. By encoding a logical Bell state, we have demonstrated entanglement between the two logical qubits. From the state tomography we have revealed logical fidelity from 96.6% to 99.9% for all characterized logical states, which is in line with prior results using the same code on a neutral atom [32] and superconducting

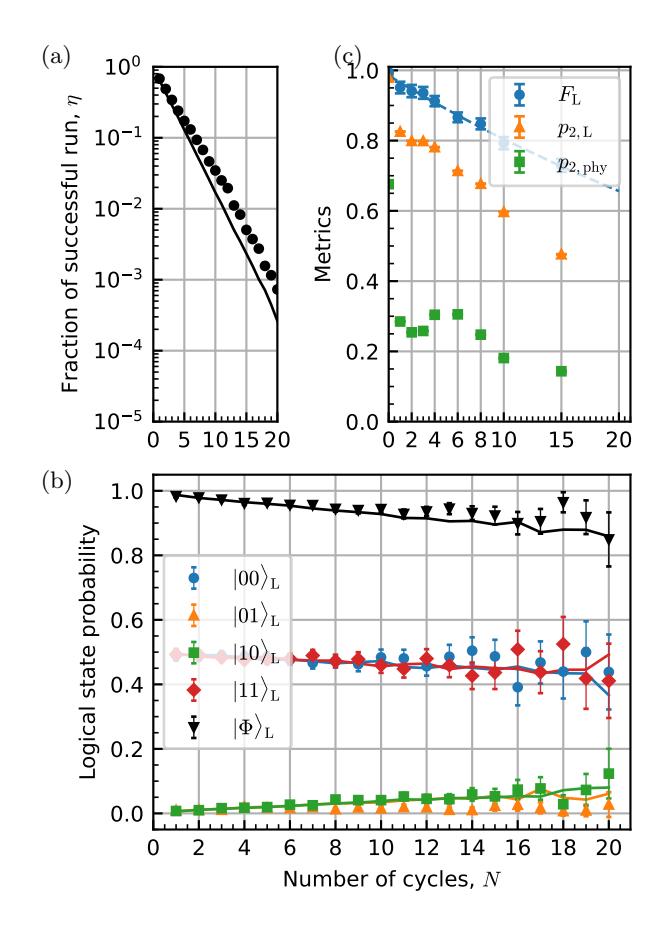


FIG. 4. Repeated error detection for a logical Bell state. a) Fraction of successful run during repeated error detection cycles. b) Logical state probability measured (markers) and simulated (solid lines) over number of cycles for the states $|00\rangle_{\rm L}$, $|01\rangle_{\rm L}$, $|10\rangle_{\rm L}$, $|11\rangle_{\rm L}$ and $|\Phi\rangle_{\rm L}$. The whiskers represent one standard deviation considering a binomial distribution of η_N . Time is calculated from the duration of the error detection cycle. c) Logical fidelity $F_{\rm L}$, logical purity $p_{2,\rm phy}$ of the Bell state given by classical shadow.

qubits [19] platform. We have demonstrated preservation of the logical state up to 20 cycles with logical life time $>100~\mu s$, which is above the life-time of the best physical components of the QPU. The observed logical error rate, characterized by a logical error per cycle ranging from 0.25(2)~% to 0.91(3)~% is below error probability of the best used physical CZ gate. The number of logical qubits and their performance exceeds the one demonstrated using surface code in Ref. [7].

In addition to good coherence of the physical qubits, the performance of the code has been enabled by the high connectivity of the star topology and parallel operation of X and Z ancilla qubits. We have used a resonator as a central element, mapped the data qubit parity to the resonator state with CZ gates and swapped ancilla qubit and resonator states using MOVE operations. Our implementation only needs two MOVE operations per ancilla and error detection cycle and which is a modest additional circuit depth. As shown in the error budget in App. I, the MOVE operation contribution to the overall rejection rate and logical error rate is very small. Furthermore, this overhead does not scale with increasing number of data qubits. On the other hand MOVE operation and central resonator are what enable the use of color code.

ACKNOWLEDGMENTS

Correspondence regarding $_{
m this}$ work should be addressed to Florian Vigneau (florian.vigneau@meetiqm.com), Johannes Hein-(johannes@meetigm.com) or Frank Deppe (frank.deppe@meetigm.com). We thank Brian Tarasinski, Amin Hosseinkhani, Olexiy Fedorets, Jakub Mrożek and Antti Vepsäläinen for usefull discussions. work was supported by the German Federal Ministry of Education and Research through the projects DAQC (13N15686), QSolid (13N16155) and Q-Exa (13N16065).

M. E. Beverland, P. Murali, M. Troyer, K. M. Svore, T. Hoefler, V. Kliuchnikov, G. H. Low, M. Soeken, A. Sundaram, and A. Vaschillo, Assessing requirements to scale to practical quantum advantage, arXiv preprint arXiv:2211.07629 (2022).

^[2] J. Preskill, Beyond NISQ: The Megaquop Machine (2025), arXiv:2502.17368 [quant-ph].

^[3] D. Gottesman, Stabilizer Codes and Quantum Error Correction, Ph.D. thesis, California Institute of Technology (1997).

^[4] B. M. Terhal, Quantum error correction for quantum memories, Rev. Mod. Phys. 87, 307 (2015).

^[5] A. G. Fowler, M. Mariantoni, J. M. Martinis, and A. N. Cleland, Surface codes: Towards practical large-scale quantum computation, Physical Review A—Atomic, Molecular, and Optical Physics 86, 032324 (2012).

^[6] S. B. Bravyi and A. Y. Kitaev, Quantum codes on a

lattice with boundary, arXiv preprint quant-ph/9811052 (1998).

^[7] C. K. Andersen, A. Remm, S. Lazar, S. Krinner, N. Lacroix, G. J. Norris, M. Gabureac, C. Eichler, and A. Wallraff, Repeated quantum error detection in a surface code, Nature Physics 16, 875 (2020).

^[8] Google Quantum AI and Collaborators, Quantum error correction below the surface code threshold, Nature, 1 (2024), publisher: Nature Publishing Group.

^[9] H. Bombin and M. A. Martin-Delgado, Topological quantum distillation, Phys. Rev. Lett. 97, 180501 (2006).

^[10] S. Bravyi, A. W. Cross, J. M. Gambetta, D. Maslov, P. Rall, and T. J. Yoder, High-threshold and lowoverhead fault-tolerant quantum memory, Nature 627, 778 (2024).

^[11] J. N. Eberhardt, F. R. F. Pereira, and V. Steffan, Pruning qldpc codes: Towards bivariate bicycle codes with open

- boundary conditions (2024), arXiv:2412.04181 [quant-ph].
- [12] C. Gidney and C. Jones, New circuits and an open source decoder for the color code, arXiv preprint arXiv:2312.08813 (2023).
- [13] A. J. Landahl, J. T. Anderson, and P. R. Rice, Fault-tolerant quantum computing with color codes, arXiv preprint arXiv:1108.5738 (2011).
- [14] Y. Takada and K. Fujii, Improving threshold for fault-tolerant color-code quantum computing by flagged weight optimization, PRX Quantum 5, 030352 (2024).
- [15] L. Postler, S. Heuβen, I. Pogorelov, M. Rispler, T. Feldker, M. Meth, C. D. Marciniak, R. Stricker, M. Ringbauer, R. Blatt, et al., Demonstration of fault-tolerant universal quantum gate operations, Nature 605, 675 (2022).
- [16] L. Postler, F. Butt, I. Pogorelov, C. D. Marciniak, S. Heußen, R. Blatt, P. Schindler, M. Rispler, M. Müller, and T. Monz, Demonstration of fault-tolerant steane quantum error correction, PRX Quantum 5, 030326 (2024).
- [17] J. Beugnon, C. Tuchendler, H. Marion, A. Gaëtan, Y. Miroshnychenko, Y. R. Sortais, A. M. Lance, M. P. Jones, G. Messin, A. Browaeys, and P. Grangier, Twodimensional transport and transfer of a single atomic qubit in optical tweezers, Nature Physics 3, 696 (2007).
- [18] D. Bluvstein, S. J. Evered, A. A. Geim, S. H. Li, H. Zhou, T. Manovitz, S. Ebadi, M. Cain, M. Kalinowski, D. Hangleiter, et al., Logical quantum processor based on reconfigurable atom arrays, Nature 626, 58 (2024).
- [19] M. Takita, A. W. Cross, A. D. Córcoles, J. M. Chow, and J. M. Gambetta, Experimental demonstration of faulttolerant state preparation with superconducting qubits, Phys. Rev. Lett. 119, 180501 (2017).
- [20] C. Vuillot, Is error detection helpful on IBM 5Q chips?, Quantum Information and Computation 18, https://doi.org/10.26421%2Fqic18.11-12 (2018).
- [21] R. Harper and S. T. Flammia, Fault-Tolerant Logical Gates in the IBM Quantum Experience, Physical Review Letters 122, 080504 (2019).
- [22] C. Chamberland, A. Kubica, T. J. Yoder, and G. Zhu, Triangular color codes on trivalent graphs with flag qubits, New Journal of Physics 22, 023019 (2020), publisher: IOP Publishing.
- [23] N. Lacroix, A. Bourassa, F. J. Heras, L. M. Zhang, J. Bausch, A. W. Senior, T. Edlich, N. Shutty, V. Sivak, A. Bengtsson, et al., Scaling and logic in the color code on a superconducting quantum processor, arXiv preprint arXiv:2412.14256 (2024).
- [24] L. Vaidman, L. Goldenberg, and S. Wiesner, Error prevention scheme with four particles, Physical Review A 54, R1745 (1996).
- [25] M. Grassl, T. Beth, and T. Pellizzari, Codes for the quantum erasure channel, Physical Review A 56, 33 (1997).
- [26] D. W. Leung, M. A. Nielsen, I. L. Chuang, and Y. Yamamoto, Approximate quantum error correction can lead to better codes, Phys. Rev. A 56, 2567 (1997).
- [27] D. Gottesman, Quantum fault tolerance in small experiments, arXiv preprint arXiv:1610.03507 (2016).
- [28] D. Willsch, M. Willsch, F. Jin, H. De Raedt, and K. Michielsen, Testing quantum fault tolerance on small systems, Phys. Rev. A 98, 052348 (2018).
- [29] R. Harper and S. T. Flammia, Fault-tolerant logical gates in the ibm quantum experience, Physical review letters

- **122**, 080504 (2019).
- [30] N. M. Linke, M. Gutierrez, K. A. Landsman, C. Figgatt, S. Debnath, K. R. Brown, and C. Monroe, Fault-tolerant quantum error detection, Science Advances 3, e1701074 (2017).
- [31] R. Cane, D. Chandra, S. X. Ng, and L. Hanzo, Experimental characterization of fault-tolerant circuits in small-scale quantum processors, IEEE Access 9, 162996 (2021).
- [32] M. Bedalov, M. Blakely, P. Buttler, C. Carnahan, F. T. Chong, W. C. Chung, D. C. Cole, P. Goiporia, P. Gokhale, B. Heim, et al., Fault-tolerant operation and materials science with neutral atom logical qubits, arXiv preprint arXiv:2412.07670 (2024).
- [33] M. Urbanek, B. Nachman, and W. A. de Jong, Error detection on quantum computers improving the accuracy of chemical calculations, Phys. Rev. A 102, 022427 (2020).
- [34] M. Gowrishankar, D. Claudino, J. Wright, and T. Humble, Logical error rates for a [[4, 2, 2]]-encoded variational quantum eigensolver ansatz, arXiv preprint arXiv:2405.03032 (2024).
- [35] R. S. Gupta, N. Sundaresan, T. Alexander, C. J. Wood, S. T. Merkel, M. B. Healy, M. Hillenbrand, T. Jochym-O'Connor, J. R. Wootton, T. J. Yoder, A. W. Cross, M. Takita, and B. J. Brown, Encoding a magic state with beyond break-even fidelity, Nature 625, 259 (2024).
- [36] A. Hu, J. Li, and R. Shapiro, Quantum benchmarking on the [[4, 2, 2]] code, Duke University, Department of Mathematics (2018).
- [37] B. W. Reichardt, A. Paetznick, D. Aasen, I. Basov, J. M. Bello-Rivas, P. Bonderson, R. Chao, W. van Dam, M. B. Hastings, A. Paz, et al., Logical computation demonstrated with a neutral atom quantum processor, arXiv preprint arXiv:2411.11822 (2024).
- [38] M. Renger, J. Verjauw, N. Wurz, A. Hosseinkhani, C. Ockeloen-Korppi, W. Liu, A. Rath, M. J. Thapa, F. Vigneau, E. Wybo, V. Bergholm, et al., A superconducting qubit-resonator quantum processor with effective all-to-all connectivity, arXiv preprint arXiv:2503.10903 (2025).
- [39] H.-Y. Huang, R. Kueng, and J. Preskill, Predicting many properties of a quantum system from very few measurements, Nature Physics 16, 1050 (2020).
- [40] A. Elben, S. T. Flammia, H.-Y. Huang, R. Kueng, J. Preskill, B. Vermersch, and P. Zoller, The randomized measurement toolbox, Nat. Rev. Phys. 5, 9 (2023).
- [41] R. Versluis, S. Poletto, N. Khammassi, B. Tarasinski, N. Haider, D. J. Michalak, A. Bruno, K. Bertels, and L. DiCarlo, Scalable quantum circuit and control for a superconducting surface code, Phys. Rev. Applied 8, 034021 (2017).
- [42] R. Chao and B. W. Reichardt, Quantum error correction with only two extra qubits, Phys. Rev. Lett. 121, 050502 (2018).
- [43] S. Krinner, N. Lacroix, A. Remm, A. Di Paolo, E. Genois, C. Leroux, C. Hellings, S. Lazar, F. Swiadek, J. Herrmann, et al., Realizing repeated quantum error correction in a distance-three surface code, Nature 605, 669 (2022).
- [44] A. Gilchrist, N. K. Langford, and M. A. Nielsen, Distance measures to compare real and ideal quantum processes, Phys. Rev. A 71, 062310 (2005).
- [45] C. Gidney, Stim: a fast stabilizer circuit simulator, Quantum 5, 497 (2021).
- [46] Google Quantum AI and Collaborators, Suppressing

- quantum errors by scaling a surface code logical qubit, Nature **614**, 676 (2023), publisher: Nature Publishing Group.
- [47] T. Brydges, A. Elben, P. Jurcevic, B. Vermersch, C. Maier, B. P. Lanyon, P. Zoller, R. Blatt, and C. F. Roos, Probing rényi entanglement entropy via randomized measurements, Science 364, 260 (2019).
- [48] K. J. Satzinger, Y.-J. Liu, A. Smith, C. Knapp, M. Newman, C. Jones, Z. Chen, C. Quintana, X. Mi, A. Dunsworth, C. Gidney, I. Aleiner, F. Arute, K. Arya, J. Atalaya, Babbush, et al., Realizing topologically ordered states on a quantum processor, Science 374, 1237 (2021).
- [49] M. Yu, D. Li, J. Wang, Y. Chu, P. Yang, M. Gong, N. Goldman, and J. Cai, Experimental estimation of the quantum Fisher information from randomized measurements, Phys. Rev. Res. 3, 043122 (2021).
- [50] D. Zhu, Z. P. Cian, C. Noel, A. Risinger, D. Biswas, L. Egan, Y. Zhu, A. M. Green, C. H. Alderete, N. H. Nguyen, Q. Wang, A. Maksymov, Y. Nam, M. Cetina, N. M. Linke, M. Hafezi, and C. Monroe, Cross-platform comparison of arbitrary quantum states, Nature Communications 13, 6620 (2022).
- [51] L. K. Joshi, J. Franke, A. Rath, F. Ares, S. Murciano, F. Kranzl, R. Blatt, P. Zoller, B. Vermersch, P. Calabrese, C. F. Roos, and M. K. Joshi, Observing the quantum mpemba effect in quantum simulations, Phys. Rev. Lett. 133, 010402 (2024).
- [52] V. Vitale, A. Rath, P. Jurcevic, A. Elben, C. Branciard, and B. Vermersch, Robust estimation of the quantum fisher information on a quantum processor, PRX Quantum 5, 030338 (2024).

- [53] T. I. Andersen, N. Astrakhantsev, A. H. Karamlou, J. Berndtsson, J. Motruk, A. Szasz, J. A. Gross, A. Schuckert, T. Westerhout, Y. Zhang, et al., Thermalization and criticality on an analogue-digital quantum simulator, Nature 638, 79 (2025).
- [54] B. Vermersch, A. Rath, B. Sundar, C. Branciard, J. Preskill, and A. Elben, Enhanced estimation of quantum properties with common randomized measurements, PRX Quantum 5, 010352 (2024).
- [55] A. Elben, R. Kueng, H.-Y. R. Huang, R. van Bijnen, C. Kokail, M. Dalmonte, P. Calabrese, B. Kraus, J. Preskill, P. Zoller, and B. Vermersch, Mixed-State Entanglement from Local Randomized Measurements, Physical Review Letters 125, 200501 (2020).
- [56] A. Rath, C. Branciard, A. Minguzzi, and B. Vermersch, Quantum fisher information from randomized measurements, Physical Review Letters 127, 260501 (2021).
- [57] V. Vitale, A. Elben, R. Kueng, A. Neven, J. Carrasco, B. Kraus, P. Zoller, P. Calabrese, B. Vermersch, and M. Dalmonte, Symmetry-resolved dynamical purification in synthetic quantum matter, SciPost Physics 12, 106 (2022).
- [58] K. C. Miao, M. McEwen, J. Atalaya, D. Kafri, L. P. Pryadko, A. Bengtsson, A. Opremcak, K. J. Satzinger, Z. Chen, P. V. Klimov, et al., Overcoming leakage in quantum error correction, Nature Physics 19, 1780 (2023).
- [59] J. Ghosh, A. G. Fowler, and M. R. Geller, Surface code with decoherence: An analysis of three superconducting architectures, Phys. Rev. A 86, 062318 (2012).

Appendix A: Codewords of the [4, 2, 2] code

Codewords are physical states which correspond to logical states. For [4, 2, 2] code, for our choice of stabilizers, Eq. 1, and logical operators, Eq. 2, codewords for cardinal states of the two logical qubits are

$$\begin{split} |00\rangle_{\mathrm{L}} &= (|0000\rangle + |1111\rangle)/\sqrt{2}, \\ |01\rangle_{\mathrm{L}} &= (|0011\rangle + |1100\rangle)/\sqrt{2}, \\ |10\rangle_{\mathrm{L}} &= (|0101\rangle + |1010\rangle)/\sqrt{2}, \\ |11\rangle_{\mathrm{L}} &= (|1001\rangle + |0110\rangle)/\sqrt{2}, \end{split} \tag{A1}$$

$$\begin{aligned} |++\rangle_{\rm L} &= (|++++\rangle + |----\rangle)/\sqrt{2}, \\ |+-\rangle_{\rm L} &= (|+-+-\rangle + |-+-+\rangle)/\sqrt{2}, \\ |-+\rangle_{\rm L} &= (|++--\rangle + |--++\rangle)/\sqrt{2}, \\ |--\rangle_{\rm L} &= (|-++-\rangle + |+--+\rangle)/\sqrt{2}, \end{aligned} \tag{A2}$$

$$\begin{aligned} |0+\rangle_{\rm L} &= (|++00\rangle + |++11\rangle + |--00\rangle + |--11\rangle)/2, \\ |+0\rangle_{\rm L} &= (|+0+0\rangle + |+1+1\rangle + |-0-0\rangle + |-1-1\rangle)/2. \end{aligned}$$
 (A3)

Appendix B: Error detection circuit in detail

We show in Fig. 5 error detection circuit, also shown in Fig. 1, with the horizontal axis representing the time position of each operation.

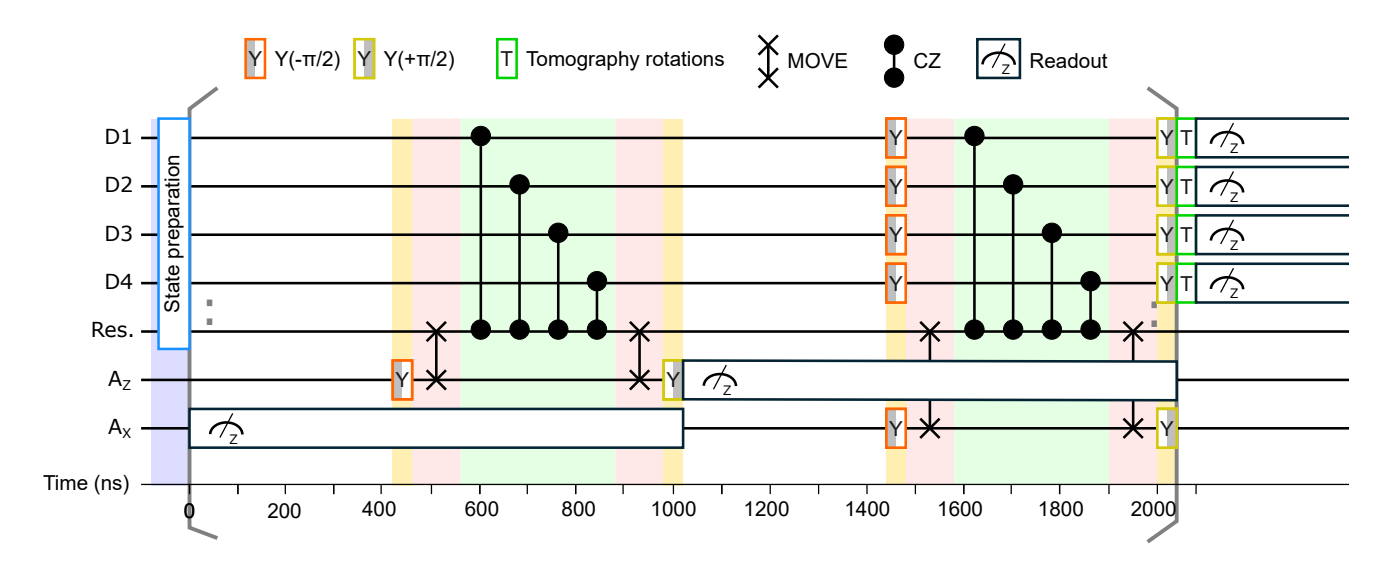


FIG. 5. Representation of the error detection circuit shown in Fig. 1 with time on horizontal axis. The background colors serve as a guide to indicate the timing and duration of each operation.

Appendix C: Logical shadow tomography

Here, we further detail the tomography protocol that we use to extract logical and physical quantum properties of interest in our experiments. The classical shadow framework has been widely used on different quantum platforms that are available today [47–53]. The state preparation of data qubits and N cycles of error detection yield a state ρ_{phy} . We then apply unitary operations $U = \bigotimes_{i=1}^4 U_i$ on the four data qubits where each U_i is uniformly sampled

in $\left\{\mathbb{I}_2, \frac{1}{\sqrt{2}} \begin{pmatrix} 1 & 1 \\ 1 & -1 \end{pmatrix}, \frac{1}{\sqrt{2}} \begin{pmatrix} 1 & -i \\ 1 & +i \end{pmatrix}\right\}$, so that $U_i^{\dagger} Z U_i = Z, X, Y$, respectively (with Z, X, Y being the Pauli matrices). These rotations are Pauli basis rotations and form an unitary 2-design.

Then, we projectively measure the rotated state $U\rho_{\text{phy}}U^{\dagger}$ in the computational basis $\{|\mathbf{d}\rangle\}$, where $|\mathbf{d}\rangle=|d_1,\ldots,d_4\rangle$ with $d_i\in\{0,1\}$. We repeat the randomized measurements N_UN_M times, where N_U is the number of sampled random unitaries $U^{(r)}$ and N_M represents the number of measurements per unitary. The resulting dataset consists of N_UN_M bitstrings, which we label as $\mathbf{d}^{(r,b)}=(d_1^{(r,b)},\ldots,d_4^{(r,b)})$ for $r=1,\ldots,N_U$ and $b=1,\ldots,N_M$. In addition to the data qubits, the experiments also involve projective measurements of the ancilla qubits, yielding

In addition to the data qubits, the experiments also involve projective measurements of the ancilla qubits, yielding stabilizer value $s_n^{\mathbf{X}}$ and $s_n^{\mathbf{Z}}$. Here, $n=1,\ldots,N$ labels the cycles of stabilizer measurements. In total, the dataset includes 2N ancilla bitstring measurements for each applied unitary $U^{(r)}$.

We then perform a postselection on the stabilizer results which reduces the total number of data qubit bitstrings to

We then perform a postselection on the stabilizer results which reduces the total number of data qubit bitstrings to N_M' for each unitary $U^{(r)}$. The post-selected bitstrings are denoted as $\mathbf{d}^{(r,b')} = (d_1^{(r,b')}, \dots, d_4^{(r,b')})$, with $r = 1, \dots, N_U$ and $b' = 1, \dots, N_M'$.

We construct, from this post-selected randomized measurement dataset, N_U classical shadows [52, 54]

$$\hat{\rho}_{\text{phy}}^{(r)} = \sum_{\mathbf{d}} \hat{P}(\mathbf{d}|U^{(r)}) \bigotimes_{j=1}^{4} \left(3 U_j^{(r)\dagger} |d_j\rangle\langle d_j| U_j^{(r)} - \mathbb{I}_2 \right)$$
(C1)

where

$$\hat{P}(\mathbf{d}|U^{(r)}) = \sum_{h'=1}^{N_M'} \frac{\delta_{\mathbf{d},\mathbf{d}^{(r,b')}}}{N_M'} \tag{C2}$$

is the estimated (noisy) Born probability from the randomized measurements dataset. This operator in Eq. (C1) is an unbiased estimator of the underlying density matrix, i.e the average over the unitaries and the bitstring measurement results in $\mathbb{E}[\hat{\rho}_{\text{phy}}^{(r)}] = \rho_{\text{phy}}$ [39]. This property indeed allows us to perform quantum state tomography from the acquired dataset.

This operator defined in Eq. (C1), allows equally to construct logical shadows for each applied random unitary $U^{(r)}$

$$\hat{\rho}_{L}^{(r)} = \sum_{i,j} \langle i | \hat{\rho}_{phy}^{(r)} | j \rangle / P_{L}$$
 (C3)

with $|i\rangle$, $|j\rangle$ being the logical basis states defined in App. A and we define the estimator of the acceptance probability $P_{\rm L} = \frac{1}{N_U} \sum_{r=1}^{N_U} {\rm Tr} \left(\hat{\rho}_{\rm phy}^{(r)} \right)$. Based on the above property of the classical shadow, it follows straightforwardly that the average over the unitaries and measurement results provide an unbiased estimation of the underlying logical density matrix $\mathbb{E}[\hat{\rho}_{\rm L}^{(r)}] = \rho_{\rm L}$ [39]. The operators defined in Eq. (C1) and Eq. (C3) are the building blocks for extracting properties of the prepared state.

We can define the shadow estimator of the fidelity F of the quantum state with respect to pure state of interest $|\psi_0\rangle$ as [54]

$$F = \frac{1}{N_U} \sum_{r=1}^{N_U} \langle \psi_0 | \, \hat{\rho}^{(r)} | \psi_0 \rangle \,, \tag{C4}$$

where $\hat{\rho}^{(r)}$ can be either be the physical $\hat{\rho}_{\text{phy}}^{(r)}$ or logical $\hat{\rho}_{\text{L}}^{(r)}$ shadow. Similarly, the unbiased estimator of the purity of the physical or logical quantum state is Refs [55–57]

$$p_2 = \frac{1}{N_U(N_U - 1)} \sum_{r_1 \neq r_2} \text{Tr} \left(\hat{\rho}^{(r_1)} \hat{\rho}^{(r_2)} \right)$$
 (C5)

where p_2 can be either be the physical $p_{2,phy}$ or logical $p_{2,L}$ purity.

Appendix D: Density matrices

Here, we provide the full density matrices from the tomography experiments.

First, we show in Fig. 6a–c the density matrices of $|00\rangle_L$, $|++\rangle_L$ and $|\Phi\rangle_L$ states obtained after 1 cycle of error detection and their respective physical states. We expect 1, 16 and 4 density matrix elements with value 1, 0.25 and

0.5 for the 3 presented states correspondingly. Due to the high fidelity, other matrix elements are small and non-systematic. In Fig. 6d–f, we present density matrices of the physical state before projection to the logical subspace. Here we expect 4, 64 and 16 matrix elements with values 0.5, 0.125 and 0.25 correspondingly. In the case of the physical density matrices, we can clearly observe effects of qubit decay, which increases ground-state probability and reduces all other expected matrix elements. However, dephasing is not as visible, which reduces off-diagonal elements compared to diagonal elements.

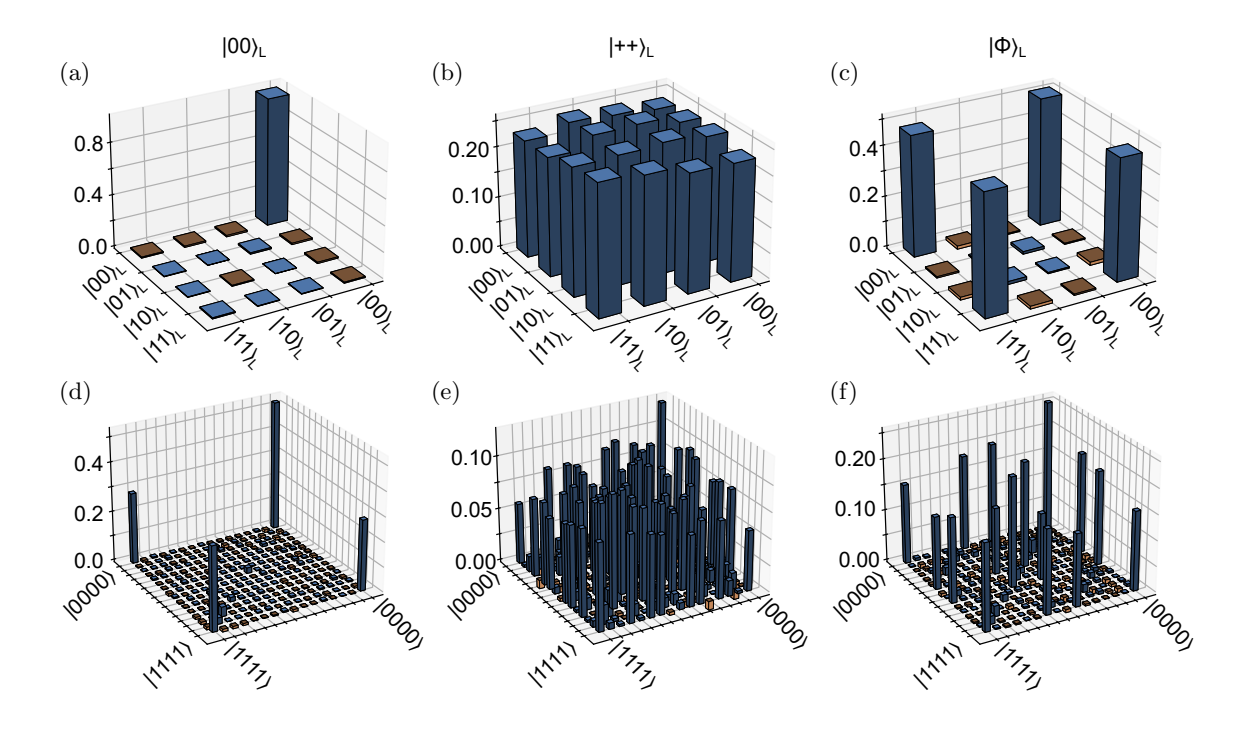


FIG. 6. Tomography for logical states $|00\rangle_{\rm L}$, $|++\rangle_{\rm L}$ and $|\Phi\rangle_{\rm L}$. a-c) represents the tomography in the logical space of the two logical qubits and c-f) represents the tomography in of the physical space of the four data qubits for the respective mentioned states starting with the initial state of $|0000\rangle$, $|++++\rangle$ and $|\Phi\rangle_{\rm L}$. Blue represents positive while yellow represents negative values of the real part of the density matrix.

For the Bell state we study the dynamics of the density matrix by presenting the density matrix after N=4,8 and 15 cycles of error detection Fig. 7. We observe an increase of unwanted diagonal elements that depolarize logical errors. We also observe an increase of $|00\rangle \langle 00|_{\rm L}$ which can be interpreted as a logical delay, which is a polarizing error.

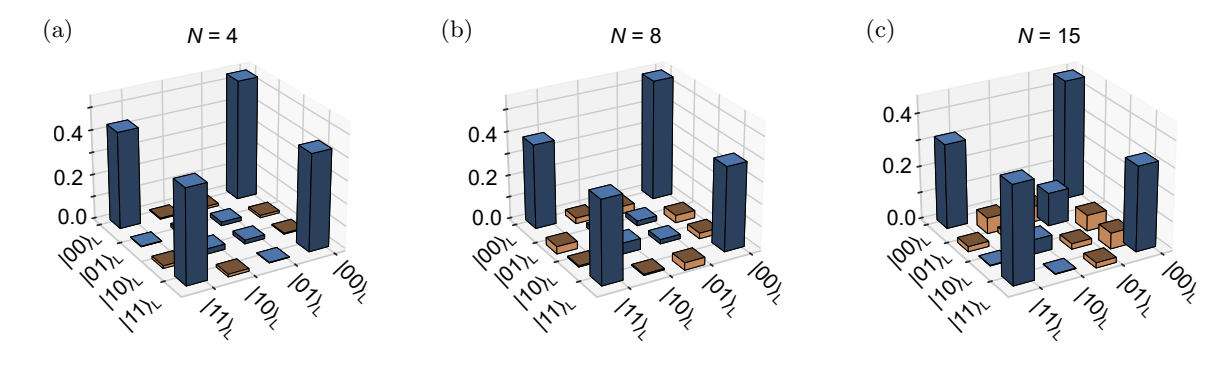


FIG. 7. Tomography of the real part of the logical Bell density matrix for different number of cycles N=4 (a), N=8 (b) and N=15 (c).

Appendix E: Syndrome detection probability

From the experiments described in Sections V and VI we already extracted the average probability of the first error happening in a given cycle $P_{\rm S}$. A complementary way to characterize the performances of quantum error detection is to study error detection, error syndrome, probability as a function of the error detection cycle number without prior postselection.

For each error detection cycle n we extract a bit d_n for either stabilizers. For our circuit, where we do not reset ancilla qubits at the start of each cycle, the stabilizer value is $s_n = +1$ if $d_n \oplus d_{n-1} = 0$ and -1 otherwise. The error syndrome $\sigma_n = (1 - s_n \times s_{n-1})/2$ is equal to 1 if a change of parity has been detected between cycles n-1 and n, and 0 otherwise.

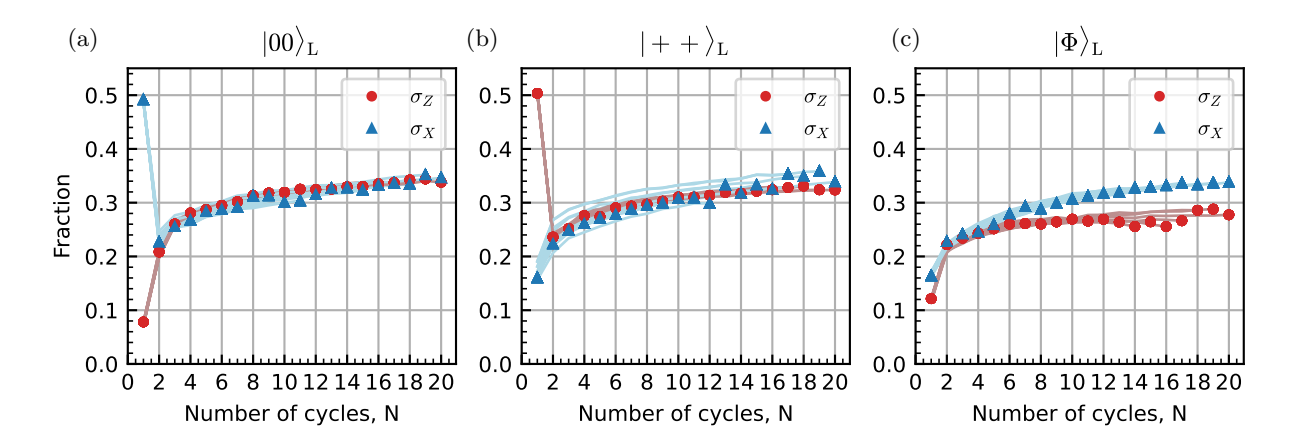


FIG. 8. Average syndrome detection $\sigma_{\rm X}(N,n)$ and $\sigma_{\rm Z}(N,n)$ for $S_{\rm X}$ and $S_{\rm Z}$ stabilizers repeated over cycles of error detection (with no postselection) for logical states $|00\rangle_{\rm L}$ (a), $|++\rangle_{\rm L}$ (b) and $|\Phi\rangle_{\rm L}$ (c). The colors dots correspond to the measurement after the N cycles and the curves to all the mid-circuit measurements happening at every $n \in [1, N[$ cycles. The results are averaged over 10^5 repetitions.

We observe, that after the first cycle, the stabilizer that is not of the encoded basis triggers an error syndrome for about half of the experimental runs, see Fig. 8a,b, as expected from probabilistic encoding. Due to the deterministic encoding, both detection probabilities are low for the logical Bell state, see Fig. 8c. After the first cycle, the average syndrome detection reaches 0.3, which is comparable to $1-P_{\rm S}$ observed in other experiments described in the main text. There is also a trend of increasing detection probability which we attribute this trend to leakage accumulation [58], see Section F.

Appendix F: Leakage detection and postselection

To study possible reasons for detection probability dynamics, we measure the leakage accumulation in the qubits during the error detection cycles. While the rest of the experiments of this paper are done with a two state classifier, we use here a three state classifier and optimize the readout parameters to differentiate the three qubit states $|0\rangle$, $|1\rangle$ and $|2\rangle$. In this experiment, the correct assignment probability is > 99 % for state $|0\rangle$ (except D2 : > 97 %), > 94 % for state $|1\rangle$, and > 93 % for state $|2\rangle$ (except A_X : > 84%). We account a qubit measured in the state $|2\rangle$ as leakage.

We execute the quantum error detection protocol with the three state classifier. In Fig. 9a, we show the error syndromes of both $S_{\rm X}$ and $S_{\rm Z}$ stabilizers after rejecting any run that contains $|2\rangle$ results. After a few cycles the syndrome fraction plateau, while on the other hand, the syndrome fraction keep increasing in Fig. 8 where leakage is not rejected. In addition, compare the fraction of leakage detected for ancilla qubits, see Fig 9b, and data qubits, Fig 9c. We see a steady increase of leakage fraction with N (and n) for both $A_{\rm X}$ and $A_{\rm Z}$. On the other hand, the leakage remains low in data qubit. Therefore, we hypothesise that leakage in this QPU mainly arises from the readout pulses or MOVE gates. We observe an irregularly high leakage for $A_{\rm X}$ and D3 between cycle 8 and cycle 18 that could be explained by some drift of the device parameters during the long measurement time of the experiment.

Note that as we use a two state classifier in the rest of the experiments of this paper, leakage cannot be detected. As the readout parameters are optimized to best distinguish the states $|0\rangle$ and $|1\rangle$ in the IQ plane, the $|2\rangle$ states are mostly classified as $|1\rangle$. Therefore, leakage in ancilla qubits would likely be interpreted as an error in the stabilizer

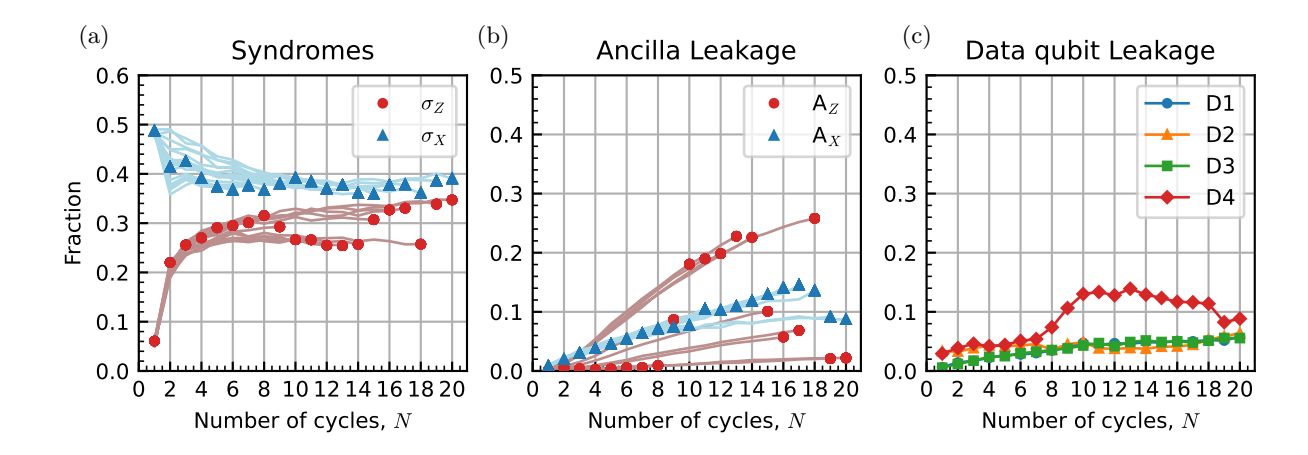


FIG. 9. Measurement of leakage during repeated error detection cycles. Error syndromes after rejecting the results that contains leakage. The colors dots correspond to the measurement after the N cycles and the curves to all the mid-circuit measurements happening at every $n \in [1, N-1]$ cycles. Ancilla leakage fraction measured on A_X and A_Z Data qubit leakage fraction measured on data qubits at the end of the N error detection cycles. The data qubits was prepared in the $|00\rangle_L$ state. The results are averaged over 10^4 repetitions.

measurement and discarded by the postselection. For this reason, we believe that leakage does not affect the logical error rate even when a two state classifier is used.

Appendix G: Qubit specifications

We show the main QPU characteristics in Table III. For for more detailed description of the device, calibration and benchmarking methods, and definitions, refer to Ref. [38].

Parameter	Description	QB1	QB2	QB3	QB4	QB5	QB6 Res.
f_q (GHz)	Qubit/resonator frequency	4.67	4.47	4.41	4.52	4.63	4.93 4.22
$T_{\rm q}~({ m mK})$	Qubit temperature	46.3	42.0	43.6	40.9	43.0	45.8
$F_{ m RO}$	Readout fidelity	98.3(3)	98.6(2)	98.7(3)	99.1(2)	98.9(2)	98.7(6)
$F_{\rm SQ,ind}$ (%)	Individual SQG fidelity	99.93(2)	99.94(4)	99.96(2)	99.96(1)	99.96(1)	99.89(30)
$F_{\rm SQ,sim}$ (%)	Simultaneous SQG fidelity	99.93(2)	99.92(4)	99.96(3)	99.95(1)	99.59(1)	99.87(30)
$F_{\rm m}$ (%)	Double MOVE fidelity	99.11(5)	99.34(3)	99.00(3)	99.30(3)	98.31(6)	97.95(10)
$F_{\rm cz}$ (%)	CZ fidelity	98.90(5)	98.75(4)	98.97(3)	98.04(8)	98.53(14)	96.61(5)

TABLE III. Characteristics of the QPU gates, component frequencies and temperatures, see [38].

Because the QPU characteristics fluctuate in time, the experiments described in the main text were done in two different configurations that gave better performances at the time of the experiment. Experiments described in Section V use configuration A, see Table IV, while experiments presented in Sections III, IV and VI were done in configuration B, see Table V. We give the characteristic life time of each qubits measured in within the same day as the experiments. These values are used in the respective simulations of the experiment.

Parameter Description		QB1	QB2	QB3	QB4	QB5	QB6	Res.
	Role of the qubit	A_{Z}	A_{X}	D1	D2	D3	D4	Res.
T_1 (µs)	Lifetime	26.1	44.3	64.5	38.7	40.8	29.4	5.4
$T_{2}^{*}(s)$	Dephasing time	45.1	29.1	34.7	26.4	47.2	22.8	10.3
$T_2^{\rm e}~(\mu {\rm s})$	Dephasing w.o. low freq noise contribution	51.3	52.0	45.3	36.1	56.0	39.5	

TABLE IV. Characteristics of the QPU during experiments in Section V.

Parameter	Description	QB1	QB2	QB3	QB4	QB5	QB6	Res.
	Role of the qubit	D2	D3	D4	$A_{\rm Z}$	A_{X}	D1	Res.
T_1 (µs)	Lifetime	25.7	51.2	59.1	55.0	49.0	36.4	5.7
$T_{2}^{*}(s)$	Dephasing time	37.9	30.1	31.5	19.6	60.3	42.4	11.9
$T_2^{\rm e}~(\mu {\rm s})$	Dephasing w.o. low freq noise contribution	42.4	62.2	43.0	30.8	60.9	47.8	

TABLE V. Characteristics of the QPU during experiments in Sections III, IV and VI.

Appendix H: Circuit simulation

We simulate the circuit using Stim version 1.13 [45] to obtain the simulation results in Fig. 2, 3 and 4 of the main text. We build an error model based on the error detection circuit and the performance of the QPU given in Table IV. For each gate we add a depolarization error detailed in Table VI. We also add an idling error calculated from the time qubits stay idling $T_{\rm idl}$ and its T_1 and T_2 relaxation time [59]:

$$X_{\rm error} = Y_{\rm error} = \frac{1}{4} \left(1 - \exp \left(\frac{-T_{\rm idl}}{T_1} \right) \right), \quad Z_{\rm error} = \frac{1}{2} \left(1 - \exp \left(\frac{-T_{\rm idl}}{T_2} \right) \right) - \frac{1}{4} \left(1 - \exp \left(\frac{-T_{\rm idl}}{T_1} \right) \right). \tag{H1}$$

A state preparation error $P_{\rm q}$ is added at the beginning of the circuit. It is calculated from the Boltzmann distribution $P_{\rm q} = \exp\left(-\frac{{\rm hf}}{{\rm k_B}{\rm T_q}}\right)$ using an effective temperature $T_{\rm q}$ estimated from single shot readout experiment, and frequency f_q of each component.

Operation	error probability	Stim
Unitary	$P_{\text{SQBG}} = 2(1 - F_{\text{SQ,sim}})$	${\tt DEPOLARIZE1}(P_{\rm SQBG})$
Hadamard	$P_{\text{SQBG}} = 2(1 - F_{\text{SQ,sim}})$	${\tt DEPOLARIZE1}(P_{\rm SQBG})$
MOVE	$P_{\text{MOVE}} = \frac{4}{3}(1 - \sqrt{F_{\text{m}}})$	$\texttt{DEPOLARIZE2}(P_{\text{MOVE}})$
CZ	$P_{\rm CZ} = \frac{4}{3}(1 - F_{\rm cz})$	${\tt DEPOLARIZE2}(P_{\rm CZ})$
Readout	$P_{\rm RO} = 1 - F_{\rm RO}$	${\tt DEPOLARIZE1}(P_{\rm RO})$
Idling	Eq. (H1)	$\texttt{PAULI_CHANNEL_1}(X_{\texttt{error}}, Y_{\texttt{error}}, Z_{\texttt{error}})$
Thermalization	$P_{\rm q} = \exp(-hf/k_{\rm B}T_{\rm q})$	$ exttt{X_ERROR}(P_{ ext{q}})$

TABLE VI. List of error in Stim simulations and their associated error probability for each operation of the circuit. h and $k_{\rm B}$ are the Planck and the Boltzmann constant respectively. We consider that $F_{\rm m}$ is the fidelity of the double MOVE operation.

Appendix I: Error budget

To find the dominating error source, we simulate the error detection circuit by suppressing one type of error each time. We simulate the circuit for $N = \{1, ..., 20\}$ cycle and fit the fraction of successful runs and the probability to observe the correct logical state at the end of the N cycles to obtain the rejection rate and logical error rate, respectively, Fig. 10. From these numbers, we calculate the individual contribution of each error type.

We find that the logical error rate is dominated by the contribution of the CZ gate and idling errors. This is also reflected in their contribution to the rejection rate. The readout errors affects more the rejected rate than the logical error per cycle. False positive error detection events, due to readout errors, are much more likely to happen than false negative because false negatives can be caught by the next cycle while one false positive would reject the entire run.

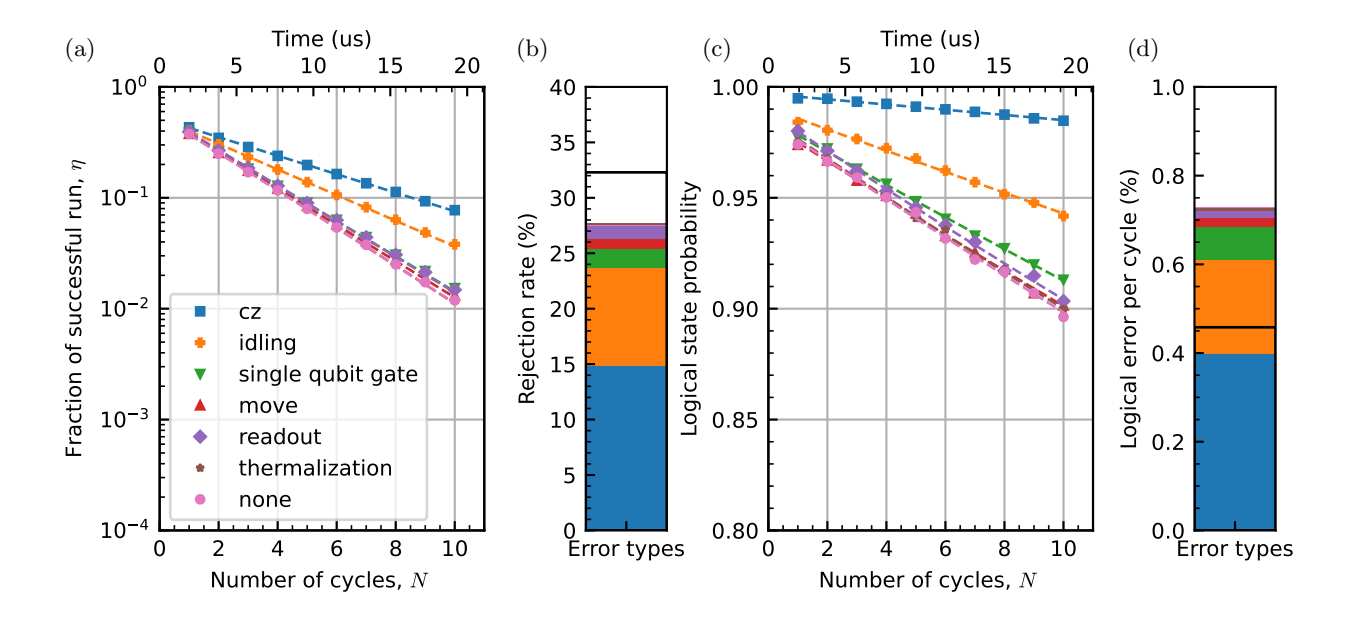


FIG. 10. Error budget made by simulating the error detection circuit by removing each time one error type indicated in the legend. "none" means that all the error type are considered. a) Fraction of successful runs where no error have been detected. Dashed line: exponential fit to extract the rejection rate. b) Individual contribution of each error type to the rejection rate. Black line rejection rate when all error types are considered. c) probability to observe the correct logical state at the end of the N cycles. Dashed line: exponential fit to extract the logical error rate for the logical state. d) Individual contribution of each error type to the logical error rate. Black line: logical error rate when all error type are considered. The simulation are calculated for the logical state $|00\rangle_{\rm L}$. The results are average over $10^5 N$ simulation runs.